Received: 5 October 2021 | Accepted: 7 October 2021

DOI: 10.1002/nano.202100306

RESEARCH ARTICLE

Nano Select WILEY

Comparison of the sputtered TiO_2 anatase and rutile thin films as electron transporting layers in perovskite solar cells

Fahimeh Shahvaranfard[1] | **Ning Li**[1,2] | **Saman Hosseinpour**[3] | **Seyedsina Hejazi**[4] | **Kaicheng Zhang**[1] | **Marco Altomare**[4] | **Patrik Schmuki**[4] | **Christoph J. Brabec**[1,2]

[1] Department of Materials Science and Engineering, Institute of Materials for Electronics and Energy Technology (i-MEET), University of Erlangen-Nuremberg, Erlangen, Germany

[2] Helmholtz Institute Erlangen-Nürnberg for Renewable Energy (HI ERN), Erlangen, Germany

[3] Institute of Particle Technology (LFG), Friedrich-Alexander-Universität-Erlangen-Nürnberg (FAU), Erlangen, Germany

[4] Department of Materials Science and Engineering, Institute for Surface Science and Corrosion WW4-LKO, University of Erlangen-Nuremberg, Erlangen, Germany

Correspondence
Fahimeh Shahvaranfard, Ning Li and Christoph J. Brabec, Department of Materials Science and Engineering, Institute of Materials for Electronics and Energy Technology (i-MEET), University of Erlangen-Nuremberg, Martensstrasse 7, 91058 Erlangen, Germany.
Email: fahimeh.shahvaranfard@fau.de

Helmholtz Institute Erlangen-Nürnberg for Renewable Energy (HI ERN), Erlangen, Germany.
Email: ning.li@fau.de; christoph.brabec@fau.de

Abstract

We examine comparatively the performance of sputtered TiO_2 rutile and anatase thin films as an electron transport layer (ETL) in $MAPbI_3$-based perovskite solar cells. Both anatase and rutile TiO_2 ETLs are deposited (on fluorine-doped tin oxide [FTO] substrates) by magnetron sputtering in the form of nanocrystalline thin films. We systematically investigate the role of crystallographic phase composition of TiO_2 ETLs on the photovoltaic performance of perovskite solar cells. The champion power conversion efficiencies (PCEs) of 18.4% and 17.7% under reverse scan mode are obtained for perovskite solar cells based on TiO_2 anatase and TiO_2 rutile ETL, respectively. The results show that the magnetron sputtering deposited ETLs differ from each other only in their phase composition while the overall performance of the devices is not greatly affected by the crystallographic phase of the TiO_2 ETLs. Our results point to an important fact that for a proper and reliable comparison between the performance of TiO_2 anatase and rutile ETLs, it is crucial to investigate films of similar morphology and structure that are synthesize under similar conditions.

KEYWORDS
magnetron sputtering, perovskite solar cell, TiO_2 anatase, TiO_2 rutile

1 | INTRODUCTION

Organic-inorganic hybrid halide perovskite solar cells (PSCs) are one of the most promising candidates for energy conversion in the photovoltaic field due to the outstanding optical and electronic properties that lead to a record efficiency of over 25%.[1–3]

In PSCs, the perovskite light absorber is sandwiched between an electron transport layer (ETL) and a hole transport layer (HTL).[4–6] ETL, as one of the key functional components in PSCs, is often comprised of a metal oxide scaffold (e.g., TiO_2,[7,8] SnO_2,[9,10] or ZnO[11,12]). Properties of ETL, such as transparency, surface roughness, electron extraction ability, and bands' position, play key roles in the

overall cell efficiency. Among different metal oxides developed as ETL, TiO_2 is the most frequent choice owing to its high chemical and photochemical stability, relatively high electron mobility, and low cost.[13–17]

Anatase and rutile are the most common crystal forms of TiO_2. Rutile is generally considered to be the thermodynamically most stable phase for bulk titania, whereas the anatase phase typically becomes more stable in nanostructured TiO_2.[18,19]

Recent works have compared anatase and rutile TiO_2 ETLs and their crystalline phase-dependent charge extraction performance as well as the effect of the TiO_2 phase on the efficiency of perovskite solar cells. For instance, Zhu et al.[20] have reported on the improvement of the device performance using anatase TiO_2 compared to the device fabricated with amorphous and rutile TiO_2. Yella et al.[21] found that nanocrystalline rutile TiO_2 performed better than a planar anatase TiO_2, an improvement which was ascribed to the large nanocrystalline rutile TiO_2/perovskite interface area for electron extraction.

In a recent work by Wang et al.,[22] TiO_2 rutile and TiO_2 anatase ETL were synthesized by two different methods; chemical bath deposition and spin coating. Their results indicated that rutile TiO_2 ETL that was synthesized by chemical bath deposition helped to improve the extraction of photoexcited electrons and decreased electron-hole recombination, due to its better conductivity, and enhanced ETL/perovskite light absorber interface compared to anatase TiO_2 ETL that was synthesized by the spin coating method. However, due to the different techniques used to produce anatase versus rutile TiO_2, it may not yield comparable ETL morphological and structural features.

In this study, we aim to systematically compare the performance of anatase TiO_2 (A-TiO_2) versus rutile TiO_2 (R-TiO_2) as ETL that are synthesized with magnetron sputtering in methylammonium lead iodide (MAPI) perovskite solar cells. Nanocrystalline anatase and rutile TiO_2 thin films are deposited on fluorine-doped tin oxide (FTO) substrates. The sputtering conditions are not only adjusted to accurately control the ETL crystallographic phase (as pure rutile or pure anatase) by tuning the chamber pressure during sputtering, but also tuned to achieve ETLs with comparable morphological and structural features, for example, in terms of surface roughness, thickness, and average crystallite size. We show that this is a key point for a proper comparison between the role of different phases TiO_2 in perovskite solar cells.

Our results, in fact, show that comparing ETLs of different phases without considering other differences in the properties of the films may be misleading in elucidating the impact of the ETL crystal structure on the overall device efficiency. Here we report that the performance of perovskite solar cells is not substantially affected by the crystallographic phase of the TiO_2 ETLs. With this work we want to draw attention to the important of a proper comparison between the performance of R-TiO_2 and A-TiO_2 as ETLs. Such a proper comparison requires that layers are (i) synthesized by the same method, and (ii) do not differ from each other in their morphological or micro-structural features. When such requirements are not met, the device performance may be simultaneously influenced by various parameters, for example, surface morphology, crystal size, and wettability, thus making a direct anatase versus rutile phase comparison unreliable.

It should be noted that here we focus on the factors that, besides crystalline structure, affect the performance of the ETLs. Indeed, high-performance light absorbers, such as mixed cation/anion hybrid perovskite materials instead of MAPI, further improves the efficiency of the device.

2 | RESULTS AND DISCUSSION

The FTO substrates coated with TiO_2 film were characterized by XRD to identify their crystallographic composition. The XRD patterns of 200 nm high pressure (HP)-TiO_2 and low pressure (LP)-TiO_2 before and after thermal treatment in air at 450°C for 1 hour are shown in Figures 1A and S1a, respectively. No information on the crystallographic phase of 30 nm sputtered TiO_2 film could be traced by XRD, probably due to the low thickness of the layers which is below the detection limit of the XRD setup used. The XRD patterns confirm mainly anatase crystalline phase composition of as-formed HP-TiO_2 and mainly rutile crystalline phase composition of as-formed LP-TiO_2 (Figure S1a). Comparing Figure S1a and Figure 1A indicates that the degree of phase crystallinity increased with thermal treatment. The XRD pattern of HP-TiO_2 shows diffraction peaks at 25.36°, 48.03°,and 54.75° which correspond to 101, 200, and 105 crystallographic planes of A-TiO_2, respectively.[23,24] The XRD pattern of LP-TiO_2 shows diffraction peaks at 27.57°, 36°, 41.37°, and 54.69° corresponding to 110, 101, 111, and 211 crystallographic planes of R-TiO_2, respectively.[23,24] The phase characterization of the 30 nm thick TiO_2 films was performed by confocal Raman spectroscopy and the corresponding spectra are provided in Figure 1B. The characteristic peaks corresponding to anatase (at 397, 516, and 638 cm^{-1})[25] appear as sharp peaks in Figure 1B whereas the characteristic peaks corresponding to rutile (at 241, 445, and ~610 cm^{-1})[25] are less pronounced, due to the large overlap with the FTO characteristic peaks (see the S1b).

Figure 2A-D shows top view and cross-sectional SEM images of 30 nm sputtered TiO_2 film on FTO substrate formed by magnetron sputtering at different chamber pressures. As shown in Figure 2A,B, the TiO_2 films form a

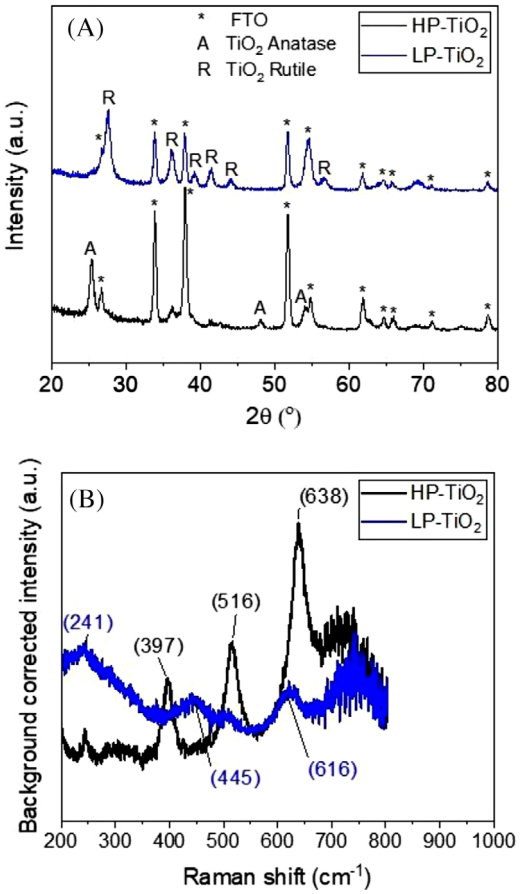

FIGURE 1 A, X-ray diffraction (XRD) patterns of 200 nm HP-TiO_2 and LP-TiO_2 on FTO. Crystallite size of anatase and rutile films was calculated from the most intense peak from XRD pattern and Scherrer equation and is ~100 nm. B, Raman spectra of the 30 nm HP-TiO_2 and LP-TiO_2 on FTO. The Raman spectra are background corrected for the FTO coated glass substrate

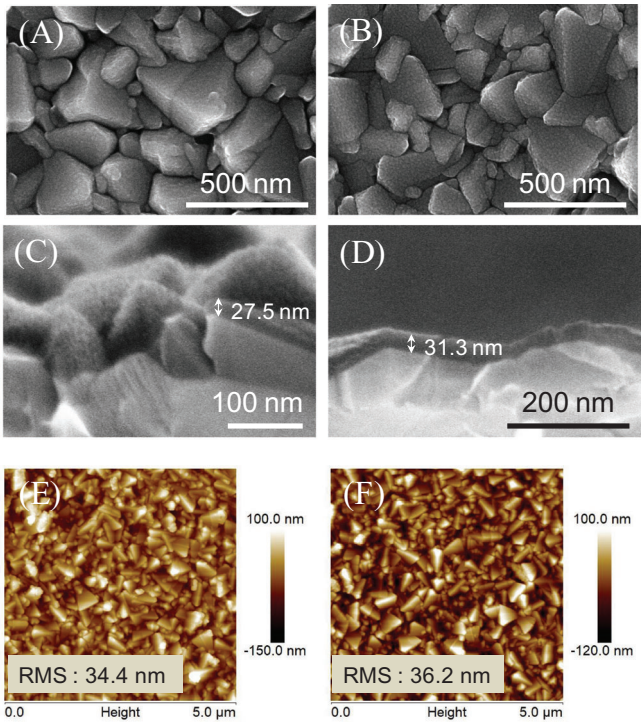

FIGURE 2 Top view and cross-sectional SEM images of (A and C) A-TiO_2, (B and D) R-TiO_2; AFM images of (E) A-TiO_2, (F) R-TiO_2 on FTO

continuous layer on the surface of the FTO regardless of the sputtering pressure. The thickness of as-sputtered layers is ~30 nm for both anatase and rutile TiO_2 films (Figure 2C,D).

To further study the surface roughness, 30 nm A-TiO_2 and R-TiO_2 films on FTO were characterized by AFM (Figure 2E,F). The root mean square (RMS) for A-TiO_2 and R-TiO_2 were 34.4 and 36.2 nm, respectively, which are virtually identical. For comparison, Figure S2 shows the top view SEM image and AFM characterization of pristine FTO. According to these results, it becomes evident that the observed surface roughness and grain size of the TiO_2 layers (Figure 2) are not entirely related to the TiO_2 layer and are predominantly affected by the FTO substrate.

The contact angle of the water droplet was measured to investigate the wettability of two types of TiO_2 films and the formation of perovskite light absorber on TiO_2 ETLs.[26,27] The contact angle of water droplets on A-TiO_2 and R-TiO_2 films is illustrated in Figure S3. The contact angle of water on A-TiO_2 and R-TiO_2 was 65.4° and 68.7°, respectively, confirming similar surface wetting properties of the two types of TiO_2 ETLs.

As shown in Figure S4, similar grain size distributions are found for perovskite layers deposited on the two ETLs. The grain size distribution statistics extracted from SEM imaging exhibited comparable feature sizes for the two samples (Figure S4) suggesting that the minor differences in roughness and wettability of TiO_2 anatase and rutile films do not impact perovskite layer growth. We conclude that the similar surface morphology and structural features of TiO_2 anatase and rutile layers that are deposited by magnetron sputtering indeed result in comparable perovskite layers morphology.

Perovskite solar cells were fabricated with a device architecture of FTO/TiO_2-ETL/$MAPbI_3$/PDCBT/MoO_x/Ag. Figure 3 shows cross-sectional SEM images of full devices fabricated with different ETLs. Cross-sectional SEM images of both devices show homogenous coverage of the TiO_2 layers.

To assess the photovoltaic performance of the PSCs, J-V curves were measured in the forward scan mode under AM 1.5 G illumination (100 mW cm^{-2}) and the results are compiled in Figure 4. The average performance parameters of both cells are summed up in Table 1. According to the results, devices based on A-TiO_2 show an average photovoltaic conversion efficiency (PCE) of 16%, a short circuit

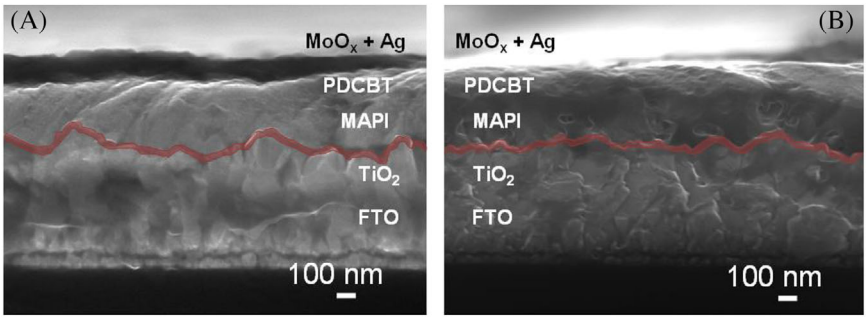

FIGURE 3 Cross-sectional SEM image of full device fabricated with (A) 30 nm A-TiO_2 (B) 30 nm R-TiO_2

current density (J_{SC}) of 22.2 mA cm^{-2}, an open circuit voltage (V_{OC}) of 1.08 V, and a fill factor (FF) of 67%. The best performing device fabricated with A-TiO_2 obtained a PCE of 17.2%, a J_{SC} of 22.6 mA cm^{-2}, a V_{OC} of 1.09 V, and a FF of 70%. For devices fabricated with R-TiO_2, an average PCE of 15.6%, a J_{SC} of 22 mA cm^{-2}, a V_{OC} of 1.07 V, and a FF of 66% are achieved. The best performing device fabricated with R-TiO_2 showed a PCE of 16.7%, a J_{SC} of 22.8 mA cm^{-2}, a V_{OC} of 1.07 V, and a FF of 68%. Figure 4C-F shows the characterization of 20 devices constructed with different TiO_2 crystallographic phase ETLs in the forward scan. It should be noted that A-TiO_2 devices show slightly higher performance parameters but not to a significant extent. To further validate the current density obtained from J-V curves, EQE measurements were performed for devices fabricated with A-TiO_2 and R-TiO_2 and the results are shown in Figure 4G. The J_{SC} values for A-TiO_2 and R-TiO_2 are 20.6 and 20.3 mA cm^{-2}, respectively, which are consistent with the average J_{SC} value from the J-V curves. As shown in Figure 4A,B, the same trend is observed in the cell performance loss for both devices constructed with A-TiO_2 and R-TiO_2 ETL under forward and reverse bias scans. This indicates that hysteresis is not impacted by using A-TiO_2 versus R-TiO_2 ETL in these perovskite solar cells.

According to these results, we found that the photovoltaic performance of the devices is not majorly affected by the crystallographic phase of the TiO_2 ETLs. To further clarify this hypothesis, we carried out further investigations on the structural and optical properties of the fabricated TiO_2 layers.

Kelvin probe measurements, which provide information on the surface electronic properties,[28,29] were employed to measure the work function of TiO_2 ETLs. Table 2 shows the average work function of 30 nm anatase and rutile layers. A minor work function difference of about 50 meV was observed for anatase (4.27 eV) versus rutile (4.22 eV), suggesting that both TiO_2 layers would follow similar energy band alignments with reference to perovskite light absorber.[30]

The optical properties of 30 nm A-TiO_2 and 30 nm R-TiO_2 on FTO were further investigated to understand whether the small differences in the blue regime of the EQE can be related to different optical properties of the interface layer. Figure 5 compares the transmission (T), reflection (R), and absorption (A) spectra that were separately measured in an integrated sphere setup. We notice that the spectra of A-TiO_2 versus R-TiO_2 are in fact very similar. Small differences in the interference peaks (best seen in the reflection curve) underline that both samples not only have a similar layer thickness but also a comparable refractive index. As a control for the accuracy of the measurements, the sum of transmittance, reflectance, and absorptance (i.e., the trend line A+T+R) is also plotted in Figure 5, showing that the deviation from 100% is less than 1.5%. Based on the optical analysis of the two TiO_2 layers, we conclude that the minor difference in cell performance or the small blue shift in the EQE are not caused by the systematically different optical properties of the TiO_2 layers. Steady-state photoluminescence (PL) spectra of perovskite (MAPI) layer on FTO, FTO/A-TiO_2 and FTO/R-TiO_2 are shown in Figure 6A. The PL results confirm an improvement in charge extraction for both A & R-TiO_2/perovskite interface compared to bare FTO/perovskite. However, both A-TiO_2 and R-TiO_2 show comparable PL quenching. The PL results further prove that anatase and rutile TiO_2 thin films act very similarly in the extraction of photo-induced electrons from the perovskite layer.

Impedance measurements were performed at 0.8 V in the dark to assess the recombination behavior of the device with A-TiO_2 and R-TiO_2 at a bias representative for the maximum power point (MPP). The Nyquist plots of devices are shown in Figure 6B. The semicircle in the Nyquist plots is discussed in terms of the most simple transient replacement circuit, where the recombination resistance is parallel to the geometric capacitance of the cell and in series with a further resistance representing all parasitic as well as internal series resistance losses.[30,31] Table S1 summarizes the extracted electrical parameters from the equivalent circuit model presented as the inset in Figure 6B. The series resistance is slightly smaller for A-TiO_2 than its R-TiO_2 counterpart; however, differences in the series resistance of 10–20% are not expected to impact the device performance. Similarly, a slightly higher recombination resistance, which is indicative of reduced recombination

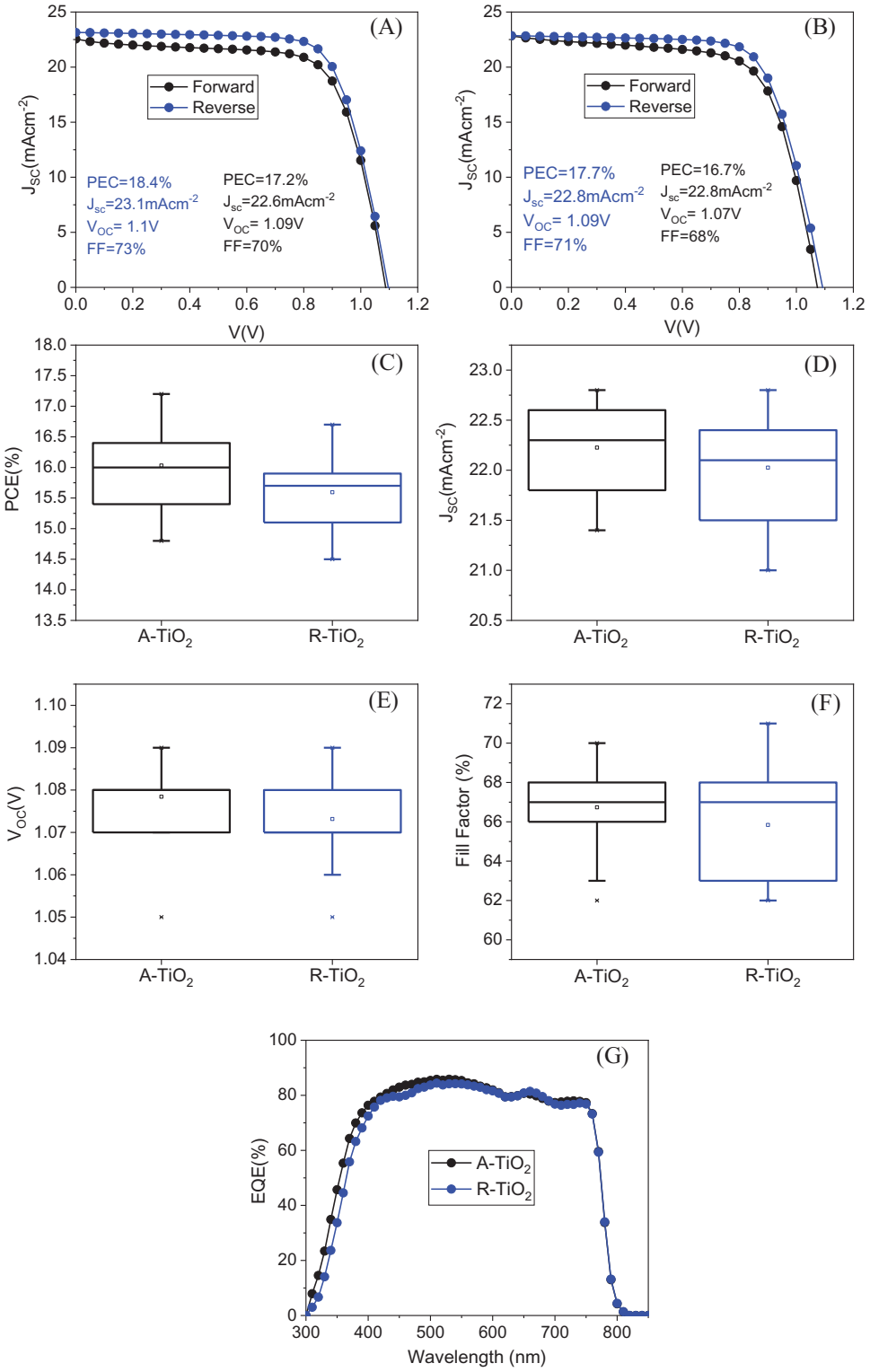

FIGURE 4 J–V curve of the best devices fabricated by (A) A-TiO_2, (B) R-TiO_2 ETLs; (C)–(F) Statistics of the photovoltaic parameters; (G) EQE spectra for devices based on A-TiO_2 and R-TiO_2

TABLE 1 Summary of the photovoltaic parameters of devices based on A-TiO_2 and R-TiO_2 ETLs

ETL construction	J_{SC} [mA cm^{-2}]	V_{OC} [V]	FF [%]	PCE_{avg} [%]	PCE_{max} [%]
A-TiO_2	22.2 ± 0.4	1.08 ± 0.009	67 ± 2.2	16 ± 0.67	17.2
R-TiO_2	22 ± 0.5	1.07 ± 0.01	66 ± 2.7	15.6 ± 0.66	16.7

TABLE 2 Work function values based on the Kelvin probe measurements in dark

Work function [eV]	
A-TiO_2	4.27 ± 0.009
R-TiO_2	4.22 ± 0.016

losses, is found for A-TiO_2, though the differences between R-TiO_2 and A-TiO_2 are again small. It is expected that sample characterizations under light also result in the comparable response from the two samples. We cannot exclude that such minor variations are originating from small variations of the properties of the sample such as slightly lower roughness, higher wettability, or a work function shift. Nevertheless, we note that loss analysis from impedance spectroscopy agrees well with the trend found from J-V analysis for A-TiO_2 versus R-TiO_2. It should be noted that besides morphology, grain size, and structure of the deposited films the characteristics of the defects within the films can also affect the performance of the deposited layers, as is shown in our previous publications.[14] However, the characterization of defect structures in the deposited films falls out of the scope of the current work.

3 | CONCLUSION

The effect of crystallographic phase composition of TiO_2 ETL on the performance of methylammonium lead iodide (MAPI) perovskite solar cells was systematically explored. Since TiO_2 thin films play a key role as the ETL in perovskite solar cells, we characterized these films with

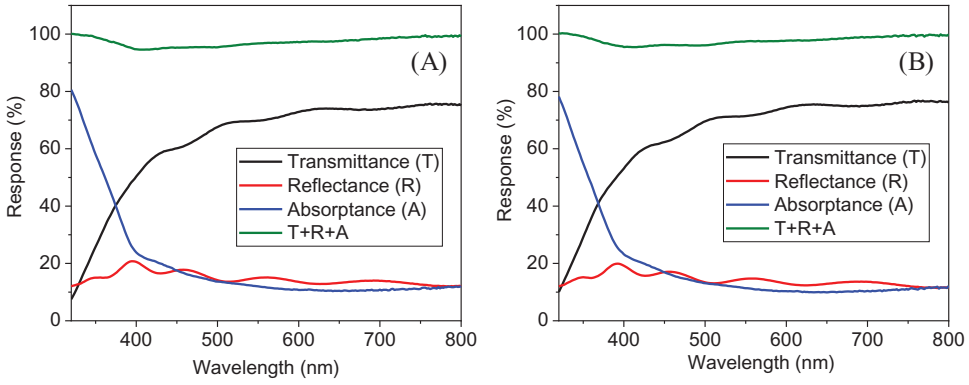

FIGURE 5 UV–Vis transmittance (T), reflectance (R) and absorptance (A) spectra of 30 nm (A) A-TiO_2 and (B) R-TiO_2 on FTO

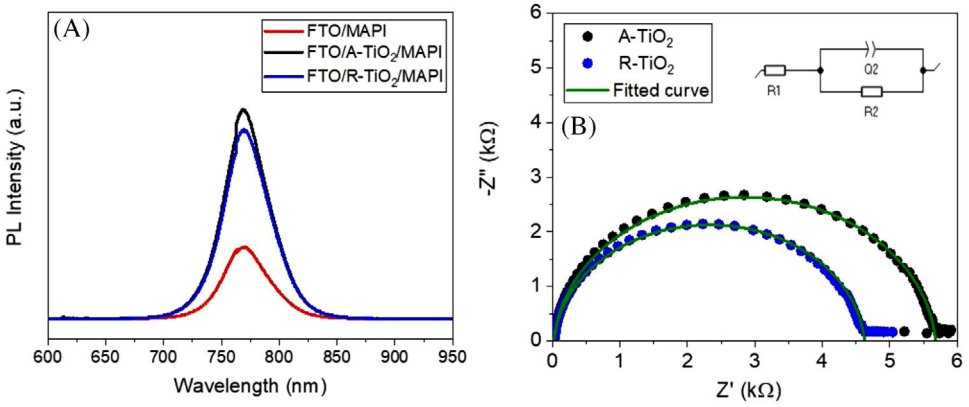

FIGURE 6 A, Steady-state PL spectra of perovskite layer on FTO, FTO/A-TiO_2 and FTO/R-TiO_2. B, Nyquist plots of full device measured in dark at an applied voltage of 0.8 V. The inset shows the equivalent circuit used for fitting

respect to their physical features, optical properties, and the ability to act as an efficient ETL in perovskite solar cells. The film deposition parameters were tuned in order to fabricate TiO_2 layers that identical in their physical and structural properties and differ only in the term of their phase composition. Our results illustrated that such anatase and rutile TiO_2 that are deposited by magnetron sputtering performed relatively comparable when processed identically. Thorough analyses explored that anatase and rutile TiO_2 layer showed only minor variations in their morphological and optical features. Accordingly, these minor variations in the film properties resulted only in minor performance differences of perovskite solar cells. Hence, our results indicate that for the proper comparison between different phases of the TiO_2 layer in an ETL, other physical and structural properties of the fabricated films should be identical, which can be achieved by controlling the fabrication parameters during film deposition.

4 | EXPERIMENTAL SECTION

4.1 | Device fabrication

FTO coated glass substrates (7 Ω m^{-2}, Solaronix) were ultrasonically cleaned in acetone, ethanol, and deionized water and were then dried with nitrogen. TiO_2 films were deposited on FTO substrates with DC magnetron sputtering in an ultrahigh vacuum chamber (Createc, SP-P-US-6 M-3Z) with pre-pump pressure of $\sim 10^{-8}$ mbar. The layers were deposited with two different chamber pressures, 2.5×10^{-3} and 2.5×10^{-2} mbar at 30 °C. A pure Ti (99.90%) was used as the target. For TiO_2 films that were deposited with different chamber pressure, the sputtering time was tuned to achieve similar layer thicknesses (~30 nm). The sputtering rates for high and low sputtering pressure were ~0.8 and ~0.95 nm min^{-1}, respectively, and the DC sputtering was performed at 150 W operating power.

The TiO_2 layers with a thickness of ~30 nm were synthesized for fabrication of perovskite solar cells and their subsequent characterization. Samples were identified based on the sputtering chamber pressure. TiO_2 films that were deposited with high sputtering pressure were labeled as HP-TiO_2 and TiO_2 films that were deposited with low sputtering pressure were labeled as LP-TiO_2. The layers were then annealed in an air furnace at 450 °C for 1 hour.

To fabricate the perovskite solar cells, the as-prepared FTO coated TiO_2 layers were transferred to a nitrogen-filled glovebox. The perovskite solution was prepared by dissolving 710 mg of PbI_2 (Lumtec) and 240 mg of CH_3NH_3I (Lumtec) in dimethylformamid (DMF) (Sigma-Aldrich) mixed with dimethylsulfoxid (DMSO) (Sigma-Aldrich) at 40°C. The perovskite precursor was spin-coated on the TiO_2 film at 4000 rpm for 15 s followed by blowing off extra solvents with a N_2 stream (gas quenching process).

The samples were then dried on a hot plate at 110°C for 10 min. As a hole transport layer, 10 mg mL^{-1} solution of poly[5,5′-bis(2-butyloctyl)-(2,2′-bithiophene)-4,4′-dicarboxylate-alt-5,5′-2,2′-bithiophene](PDCBT, 1-Material) in chlorobenzene, was deposited by spin coating on the perovskite layer at 2000 rpm for 30 s and dried at 70°C for 3 minutes. Finally, a 15 nm-thick MoO_x (Alfa Aesar) and 120 nm-thick Ag counter electrode were coated through a shadow mask (with an opening of 10.4 mm^2) on PDCBT via thermal evaporation.

4.2 | Characterization

The crystallographic composition of deposited TiO_2 ETLs was assessed by X-ray diffraction (XRD, X'pert Philips MPD diffractometer, equipped with a PanalytiCalX'celeratordetector) and confocal Raman spectrometer (LabRAM HR – Evolution, Horiba Scientific Ltd.), whereas the morphology of the deposited TiO_2 ETLs and perovskite layers was investigated by a field-emission scanning electron microscope (Fe-SEM, S4800, Hitachi). The water contact angle was measured in a static mode by OCA 20 (DataPhysics).

Current density-voltage (J-V) characterization of the solar cells was performed under simulated AM1.5G with a light intensity of 100 mW cm^{-2} which was calibrated with a Si cell with the scan rate of 2.5 V s^{-1} (step: 0.05 V). The external quantum efficiency (EQE) spectra were measured using an Enli Technology (Taiwan) EQE system (QE-R).

The work function of the layers was measured by using a Kelvin probe system in dark and the UV-vis light absorption spectra were obtained using a PerkinElmer spectroscopy system (Lambda 950 UV/VIS Spectrometer).

Steady-state photoluminescence (PL) was carried out using an Argon-ion 488-nm laser as excitation source, a Horiba monochromator and a Silicone detector. Solid state impedance spectroscopy was performed in dark at 0.8 V and in a frequency range from 1 MHz to 1 Hz by using a Zahner system.

ACKNOWLEDGEMENTS

S. Hosseinpour thanks W. Peukert and Emerging Talents Initiative (ETI) 2018/2_Tech_06, FAU, Germany, and BMBF-MSRT (grant ID: CAlSAB) for supporting his research.

Open access funding enabled and organized by Projekt DEAL.

DATA AVAILABILITY STATEMENT

The data that support the findings of this study are available from the corresponding author upon reasonable request

REFERENCES

1. N.-G. Park, K. Zhu, *Nat. Rev. Mater.* **2020**, *5*, 333.
2. A. E. Shalan, S. Narra, T. Oshikiri, K. Ueno, X. Shi, H.-P. Wu, M. M. Elshanawany, E. Wei-Guang Diau, H. Misawa, *Sustain. Energy Fuels* **2017**, *1*, 1533.
3. C. Chen, Y. Cheng, Q. Dai, H. Song, *Sci. Rep.* **2016**, *5*, 17684.
4. R. Wang, M. Mujahid, Y. Duan, Z. Wang, J. Xue, Y. Yang, *Adv. Funct. Mater.* **2019**, *29*, 1808843.
5. B. Cao, H. Liu, L. Yang, X. Li, H. Liu, P. Dong, X. Mai, C. Hou, N. Wang, J. Zhang, J. Fan, Q. Gao, Z. Guo, *ACS Appl. Mater. Interfaces* **2019**, *11*, 33770.
6. G. D. Rajmohan, F. Z. Huang, R. d'Agostino, J. du Plessis, X. J. Dai, *Thin Solid Films* **2017**, *636*, 307.
7. A. Kojima, K. Teshima, Y. Shirai, T. Miyasaka, *J. Am. Chem. Soc.* **2009**, *131*, 6050.
8. W. S. Yang, B. W. Park, E. H. Jung, N. J. Jeon, Y. C. Kim, D. U. Lee, S. S. Shin, J. Seo, E. K. Kim, J. H. Noh, S. Il Seok, *Science (80-.).* **2017**, *356*, 1376.
9. W. Ke, G. Fang, Q. Liu, L. Xiong, P. Qin, H. Tao, J. Wang, H. Lei, B. Li, J. Wan, G. Yang, Y. Yan, *J. Am. Chem. Soc.* **2015**, *137*, 6730.
10. L. Xiong, Y. Guo, J. Wen, H. Liu, G. Yang, P. Qin, G. Fang, *Adv. Funct. Mater.* **2018**, *28*, 1802757.
11. D.-Y. Son, J.-H. Im, H.-S. Kim, N.-G. Park, *J. Phys. Chem. C* **2014**, *118*, 16567.
12. J. Kim, G. Kim, T. K. Kim, S. Kwon, H. Back, J. Lee, S. H. Lee, H. Kang, K. Lee, *J. Mater. Chem. A* **2014**, *2*, 17291.
13. S. Zhang, L. Lei, S. Yang, X. Li, Y. Liu, Q. Gao, X. Gao, Q. Cao, Y. Yu, *Chem. Lett.* **2016**, *45*, 592.
14. F. Shahvaranfard, M. Altomare, Y. Hou, S. Hejazi, W. Meng, B. Osuagwu, N. Li, C. J. Brabec, P. Schmuki, *Adv. Funct. Mater.* **2020**, *30*, 1909738.
15. A. Huang, L. Lei, J. Zhu, Y. Yu, Y. Liu, S. Yang, S. Bao, X. Cao, P. Jin, *ACS Appl. Mater. Interfaces*, **2017**, *9*, 2016.
16. C. Liang, Z. Wu, P. Li, J. Fan, Y. Zhang, G. Shao, *Appl. Surf. Sci.* **2017**, *391*, 337.
17. X. Yao, J. Liang, Y. Li, J. Luo, B. Shi, C. Wei, **2017**, 1700008.
18. P. Roy, S. Berger, P. Schmuki, *Angew. Chem. Int. Ed.* **2011**, *50*, 2904.
19. S. J. Smith, R. Stevens, S. Liu, G. Li, A. Navrotsky, J. Boerio-Goates, B. F. Woodfield, *Am. Mineral.* **2009**, *94*, 236.
20. L. Zhu, Q. Lu, L. Lv, Y. Wang, Y. Hu, Z. Deng, Z. Lou, Y. Hou, F. Teng, *RSC Adv.* **2017**, *7*, 20084.
21. A. Yella, L.-P. Heiniger, P. Gao, M. K. Nazeeruddin, M. Grätzel, *Nano Lett.* **2014**, *14*, 2591.
22. Y. Wang, J. Wan, J. Ding, J. S. Hu, D. Wang, *Angew. Chemie - Int. Ed.* **2019**, *58*, 9414.
23. K. Thamaphat, P. Limsuwan, B. Ngotawornchai, *Kasetsart J. (Nat. Sci.)* **2008**, *42*, 357.
24. K. Sakurai, M. Mizusawa, *Anal. Chem.* **2010**, *82*, 3519.
25. D. Tuschel, *Spectroscopy* **2019**, *34*, 10.
26. T.-C. MikhailPylnev, A. MariaBarbisan, *Appl. Surf. Sci.* **2021**, 541.
27. X. Huang, Z. Hu, J. Xu, P. Wang, J. Zhang, Y. Zhu, *Electrochim. Acta* **2017**, *231*, 77.
28. X. Zhang, Y. Lin, D. He, J. Zhang, Z. Fan, T. Xie, *Chem. Phys. Lett.* **2011**, *504*, 71.
29. R. Cohen, L. Kronik, A. Shanzer, D. Cahen, A. Liu, Y. Rosenwaks, J. K. Lorenz, A. B. Ellis, *J. Am. Chem. Soc.* **1999**, *121*, 10545.
30. W. Zeng, X. Liu, H. Wang, D. Cui, R. Xia, Y. Min, *Thin Solid Films* **2017**, *629*, 11.
31. H. Kim, I. Mora-Sero, V. Gonzalez-Pedro, F. Fabregat-Santiago, E. J. Juarez-Perez, N. Park, J. Bisquert, *Nat. Commun.* **2013**, *4*, 2242.

SUPPORTING INFORMATION

Additional supporting information may be found in the online version of the article at the publisher's website.

How to cite this article: F. Shahvaranfard, N. Li, S. Hosseinpour, S. Hejazi, K. Zhang, M. Altomare, P. Schmuki, C. J. Brabec. *Nano Select*. **2022**, *3*, 990. https://doi.org/10.1002/nano.202100306